Structural Safety 115 (2025) 102598

Contents lists available at ScienceDirect

Structural Safety

journal homepage: www.elsevier.com/locate/strusafe

Seismic risk and failure modes assessment of steel BRB frames under earthquake sequences

Fernando Gutiérrez-Urzúa [a,b,*], Fabio Freddi [a], Enrico Tubaldi [c]

[a] Dept. of Civil, Environmental & Geomatic Engineering, University College London, London, UK
[b] AtkinsRéalis, Epsom, UK
[c] Department of Civil & Environmental Engineering, University of Strathclyde, Glasgow, UK

ARTICLE INFO

Keywords:
Buckling-restrained braces
Low-cycle fatigue
Residual deformation
Risk assessment
Earthquake sequences
Pulse-like and non-pulse-like ground motions

ABSTRACT

Buckling-Restrained Braces (BRBs) are characterized by steady and nearly symmetric hysteretic loops, providing large energy dissipation capacity under strong earthquakes. These devices are designed to sustain a specified maximum ductility demand and, if not properly designed, may fail due to excessive inelastic deformations. Moreover, their low post-yielding stiffness may lead the structure to large residual inter-story drifts at the end of the earthquake motion, and the cumulative ductility demand due to repeated plastic excursions may lead to low-cycle fatigue failure of the device core. The risk of reaching either of these failure modes is exacerbated when considering multiple earthquakes. Although BRBs are designed to function as a fuse element, there is a lack of consensus on the criteria for replacement, particularly when large residual deformations are not observed. Recent studies have suggested that BRBs can withstand several loading cycles before developing low-cycle fatigue rupture; thus, the decision to replace a BRB after a single ground motion may be overly conservative. The present study investigates the likelihood of BRBs reaching these failure modes within a stochastic framework that considers the probability of occurrence of multiple earthquakes during the structure's lifetime. For this purpose, two steel Moment Resisting Frames (MRFs) retrofitted with BRBs are numerically modeled in OpenSees and subjected to the cumulative demand from hazard-consistent multiple earthquake sequences. The demand values are compared with multiple capacity models for low-cycle fatigue in the BRB core, as well as conventional limits for residual drifts and other failure modes. The outcomes of this study suggest that the risk of developing low-cycle fatigue in BRBs is negligible, even when multiple ground motions are considered, while other failure modes are significantly more likely to occur, particularly when the structures are subjected to pulse-like ground motions.

1. Introduction

Buckling-Restrained Braces (BRBs) have proven to be an effective solution to increase the seismic performance of new and existing building structures. Unlike conventional braces, BRBs avoid buckling of the bracing elements under compression loads by encasing a steel core in an unbonded restraining sleeve, thus allowing the development of large plastic deformation both in tension and compression with nearly symmetric hysteretic loops [1–5]. When used as a retrofitting element within Moment Resisting Frames (MRFs), BRBs work in parallel with the moment-transferring beam-to-column connections, thus forming a mechanism similar to a dual structure [6–8]. In this scenario, the Buckling-Restrained Braced Frame (BRBF) provides significant lateral stiffness and large hysteretic energy dissipation capacity [9], while the MRF may provide the elastic potential energy required to recenter the structure.

In a capacity design philosophy, BRBs are designed to function as fuse elements by enabling the yielding of the steel core as a means for providing energy dissipation capabilities while reducing the plastic demands in the rest of the structure. Therefore, in case of significant damage, BRBs can be replaced [10–12], and a performance similar to the pre-earthquake one can be obtained under future earthquakes [13]. In order to guarantee the required performance in the BRBs, most modern design codes require the devices to pass qualification tests to ensure that the ductility capacity exceeds the design ductility demand under predefined loading scenarios [14]. The AISC 341-16 [15], for example,

---

* Corresponding author at: Dept. of Civil, Environmental & Geomatic Engineering, University College London, London, UK.
E-mail address: f.urzua@ucl.ac.uk (F. Gutiérrez-Urzúa).

https://doi.org/10.1016/j.strusafe.2025.102598
Received 27 August 2024; Received in revised form 23 February 2025; Accepted 24 March 2025

requires the BRB to withstand a loading protocol that includes deformation cycles with an amplitude of up to twice the one corresponding to the design story drift, and a minimum Cumulative Plastic Deformation (CPD) of 200 times the yield deformation. These testing requirements are consistent with the observations from many experimental and analytical studies [13,16,17], as CPD demands above the 200 threshold have not been reported after a single ground motion, even when considering the Maximum Considered Earthquake (MCE). Previous research work [13,18–21] has demonstrated that the probability of low-cycle fatigue failure after a single ground motion is negligible. However, very few researchers have investigated the cumulative effects of earthquake sequences in the BRBs; thus, it is unclear if these devices are able to sustain repeated earthquakes and if they should be replaced after a single ‘strong’ event.

Many authors have assessed the low-cycle fatigue capacity of BRBs and proposed capacity models based on previous experiments [18–22]. Some of these capacity models are calibrated via regression analyses that consider the BRB material and geometric properties as independent variables [22]. On the other hand, most of the models (*e.g.*, [18–21]) are derived through Coffin-Manson relationships [23,24], built by considering the results of multiple BRB tests carried out at different loading amplitudes. Yet, the application of these constant-amplitude models for assessing the likelihood of low-cycle fatigue failure under earthquake hazard is not straightforward, as a consequence, a probabilistic approach must be considered to account for the stochastic nature of the variable-amplitude deformation histories induced by potential earthquakes.

In addition, previous studies have highlighted that BRBs are susceptible to significant residual deformations due to their low post-yielding stiffness [9,25], which may be detrimental to the repairability of the structure [26–29], and, in some cases, may compromise structural stability [30]. Similar to the CPD, residual deformations heavily depends on the earthquakes’ characteristics. While a long ground motion with multiple ‘peaks’ (*e.g.*, one occurring in soft soil at large epicentral distances) may negatively affect the fatigue capacity, a shorter ground motion with a pulse-like shape may instead lead to excessive residual drifts. Given that both CPD and residual deformations are state-dependent quantities, their evolution should be investigated under sequential earthquakes by using a probabilistic approach [31].

Only a few authors have investigated the performance of BRBs under repeated ground motions, particularly focusing on mainshock-aftershock sequences. Hoveidae and Radpour [32] analyzed two case study BRBFs and highlighted that the increase of structural damage due to sequential ground motions strongly depends on the frequency content and intensity of the ground motions. Morfuni et al. [33] investigated the performance of a single case study BRBF subjected to assembled mainshock-aftershock sequences. The results showed a limited influence of the aftershocks in increasing the CPD demand. Veismoradi et al. [34] numerically investigated various case study structures, and concluded that the performance of BRBFs under an aftershock largely depends on the residual drifts at the end of the mainshock. Guerrero et al. [9] studied the performance of three BRB-retrofitted structures located in the lakebed zone of Mexico City under mainshock-aftershock sequences. Their analysis focused on the comparison of the peak and residual response of the bare and retrofitted structures, while the effects on the CPDs were not investigated. Although all the above studies considered the impact of mainshock-aftershock sequences, none of them assessed the effects of the multiple mainshocks that the structure may experience during its life cycle. Moreover, none of them considered the pulse characteristics of the ground motions, which may affect which specific failure mode is reached first.

This study advances knowledge in this area by evaluating the likelihood of various failure modes in steel BRBs, which are typically treated in isolation (*i.e.*, independently of one another). The failure modes considered include peak transient demands on BRBs and MRF structural elements, low-cycle fatigue rupture of BRBs, and excessive residual drifts. These modes should not be considered independent, as the occurrence of one may preclude the occurrence of another.

Given the cumulative nature of certain BRB-related failures (*e.g.*, residual deformation, low-cycle fatigue rupture), and the potential state-dependency of the structural response (*e.g.*, due to BRB isotropic hardening or structural damage) this assessment is conducted under multiple earthquake scenarios. Ground motion records are sampled using an algorithm that is based on a widely used Poisson model for earthquake occurrences and preserves the probabilistic distribution of the hazard intensity while minimizing excessive accelerogram scaling.

Two steel MRFs retrofitted with short BRBs (*i.e.*, an elastic brace connected in series with a BRB device) are selected for case study purposes. The two case studies represent different retrofit designs of the same existing MRF, considering different design objectives. The case studies are numerically simulated and analyzed in OpenSees [35] under hazard-compatible earthquake sequences, incorporating both pulse-like and non-pulse-like records. This approach enables an evaluation of how ground motion characteristics influence failure modes.

Additionally, the study examines the impact of the ground motion characteristics on the probability of occurrence of specific failure modes by comparing demand values against existing BRB capacity models. In particular for low-cycle fatigue rupture, six experimentally calibrated models are considered. The findings offer valuable insights into the performance and reliability assessment of BRB-equipped structures following multiple earthquake events and provide guidance on potential decision-making criteria for BRB replacement.

2. Stochastic framework

This section describes the methodology employed to assess the probability of seismic-induced failures of a structure, considering the potential occurrence of multiple earthquakes characterized by different intensities during a time interval t_L. The procedure is successively applied to the case study Moment Resisting and Buckling-Restrained Braced Frames (MR-BRBFs), where the time interval t_L is assumed to coincide with the structure’s lifespan and where the structure’s failure could be related to different failure modes.

Let D_i and C_i denote respectively the demand and capacity values corresponding to the *i*-th Engineering Demand Parameter (EDP$_i$) used to monitor a specific failure mode *i*. The probability of failure under the *i*-th failure mode during t_L can be expressed as:

$$P(D_i \geq C_i|t_L) = \sum_{n=1}^{\infty} P(D_i \geq C_i|N = n) \bullet P[N = n|t_L] \tag{1}$$

where $P(D_i > C_i|N = n)$ denotes the probability that the demand D_i exceeds the capacity C_i, conditional to a number of events $N = n$, and $P[N = n|t_L]$ denotes the probability of having $N = n$ shocks in t_L.

In this study, only mainshock events are considered, and $P[N = n|t_L]$ is described by a time-invariant Poisson model as follows:

$$P[N = n|t_L] = \frac{(\lambda_0 t_L)^n}{n!} e^{-\lambda_0 t_L} \tag{2}$$

where λ_0 denotes the site-specific mean annual frequency of occurrence of earthquake events of any intensity. The use of a Poisson model to describe the occurrence of mainshock events is well documented in literature (*e.g.*, [31]). The use of such model relies on the assumption that mainshock events alone can be descriptive of the site seismicity, with foreshocks and aftershocks disregarded through a de-clustering procedure which may induce a bias on the hazard function for the site [36]. Previous research works have proposed advanced methods to provide a more accurate representation of site seismicity, *e.g.*, site-specific Probabilistic Seismic Hazard Analyses (PSHA) or Epidemic-Type Aftershock Sequences (ETAS) [36]. Nonetheless, a Poissonian model is employed herein as the purpose of this work is to compare the seismic risk associated with specific failure modes in steel BRBFs, rather than to provide risk estimates for a building at a specific location.

The earthquake events within a sequence have different characteristics in terms of intensity, frequency content, and duration. The seismic intensity is described by an Intensity Measure (*IM*) and by a site-specific hazard function $\lambda_{IM}(im)$, which denotes the mean annual frequency of events with intensity $IM > im$:

$$\lambda_{IM}(im) = \lambda_0 P(IM > im) \tag{3}$$

The Cumulative Distribution Function (CDF) of the *IM* at each earthquake occurrence is:

$$F_{IM}(im) = P(IM \leq im) = 1 - \frac{\lambda_{IM}(im)}{\lambda_0} \tag{4}$$

In order to evaluate $P(D_i \geq C_i | N = n)$ for a structure and failure mode of interest, a Monte Carlo approach is adopted. For this purpose, n_{seq} sequences of earthquakes are generated, each characterized by n_{max} ground motion records, where n_{max} is a number sufficiently high to result in a negligible value of $P[N = n_{max} | t_L]$. The values of the intensity im_{jk} of the j-th earthquake ($j = 1,2,\ldots,n_{max}$) within the k-th sequence ($k = 1,2,\ldots,n_{seq}$) are obtained by repeatedly sampling from the CDF in Eq. (4). Ground motion records compatible with the sampled im_{jk} values are selected from the available database of ground motion records. Non-linear time-history analyses are subsequently carried out for the selected case study structure to evaluate the peak and cumulative values of the EDPs of interest.

Let $D_{i,kn}$ denote the maximum value the i-th EDP of interest observed at the end of n earthquakes within the k-th sequence, and $C_{i,m}$ the capacity values sampled from a probabilistic distribution of capacity (or a deterministic capacity value, depending on the failure mode), for $m = 1,2,..,n_{sam}$. The following expression is used to evaluate $P(D_i \geq C_i | N = n)$:

$$P(D_i \geq C_i | N = n) = \sum_{k=1}^{n_{seq}} \sum_{m=1}^{n_{sam}} \frac{I\left[D_{i,kn} \geq C_{i,m} | N = n\right]}{n_{sam} \bullet n_{seq}} \tag{5}$$

where I is the indicator function, assuming the value of one if $D_{i,kn} \geq C_{i,m}$, and zero otherwise. It is noteworthy that n_{seq} and n_{sam} must be sufficiently high to obtain accurate estimates of the failure probability conditional to the occurrence of n earthquakes.

3. Case study structures and numerical modeling

3.1. Case study structures and BRBs design

The present research considers two dual MR-BRBFs as case study structures. The MRF is the same for the two systems and is based on the North-South external frame of the pre-Northridge Boston 3-story steel building designed within the SAC Steel Project [37]. The BRBFs are consistent with two of the retrofit designs by Gutiérrez-Urzúa and Freddi [38], namely R-4 and R-6, which are characterized by different performance targets and design criteria for the BRBs. These retrofitting schemes consist of two BRBs per story in a chevron configuration, as shown in Fig. 1. The material of beams and columns is based on the ASTM A572 standard, Grade 50, Group (1) ($f_y = 1.1 \times 344.74$ MPa; $E = 199.95$ GPa). The BRBs core is characterized by Young's modulus $E = 199.95$ GPa and yielding strength $f_y = 322$ MPa.

The BRB retrofitting schemes were designed such that all BRB devices reached a ductility value of 20 at the drift demands obtained with a 975-year return period spectrum. This return period is associated with the Collapse Prevention (CP) performance level in the ASCE 41–17 [39]. The design procedure was based on an equivalent Single Degree of Freedom (SDoF) approximation [40], which involves the comparison of the structural capacity in the form of an elastic-perfectly-plastic bilinearized capacity curve, and the seismic demand in the form of an inelastic response spectrum in the displacement-acceleration space [6]. Although both retrofitting schemes are designed to comply with the same seismic demands under the same high-seismicity scenario, they are characterized by different displacement-based design objectives, which translate into BRBs with different geometric characteristics (see Table 1) and different drift demands for the MRF components. To simultaneously allow the calibration of strength, stiffness, and ductility, the BRBs are typically designed in a series arrangement of two components: the BRB device and an elastic steel brace, as shown in detail in Fig. 1. The BRB device provides the ductility capacity for the entire brace through the calibration of its core area and length, while the cross-sectional area of the elastic brace (in series with the BRB device) is designed to remain elastic and to provide the required stiffness.

The objective of the displacement-based design for R-4 is to achieve a top story drift of 0.275 m (2.3 %), which is within the range of current engineering design practices. This top story drift results from averaging the top story drift values observed at the point in which any of the MRF elements reaches the acceptance criteria for the Immediate Occupancy

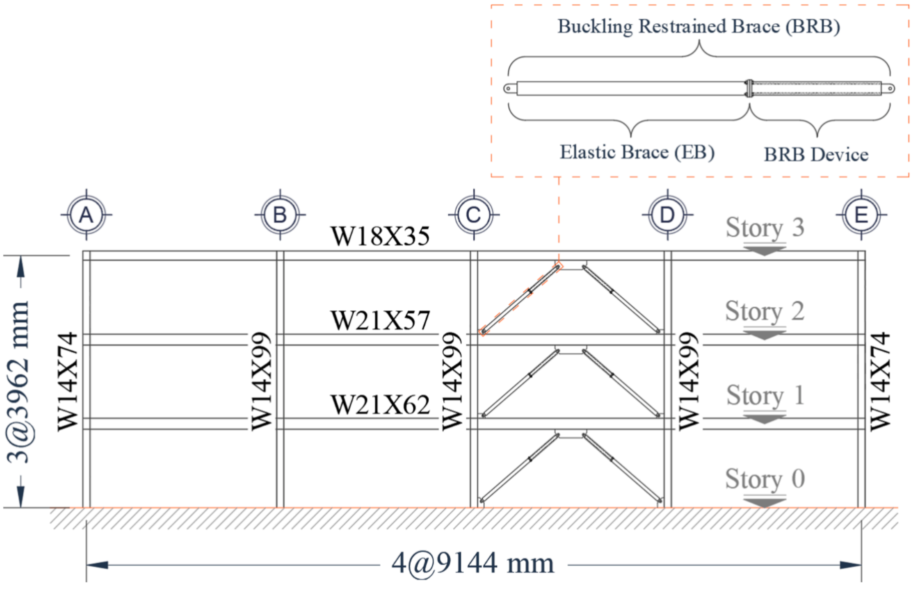

Fig. 1. Elevation of the case study structure, including cross-section details for beams and columns.

Table 1
Dimensions of the BRBs, as outlined by Gutiérrez-Urzúa and Freddi [38].

Retrofitting case	Story	BRB device		Elastic brace
		Length [m]	Core area [mm^2]	Cross-section area [mm^2]
R-4	**1st story**	1.82	4344	15,878
	2nd story	2.30	3722	9537
	3rd story	2.13	2313	6684
R-6	**1st story**	2.54	2276	4923
	2nd story	3.21	1950	2696
	3rd story	2.98	1212	1959

(IO) performance level (0.11 m) and the CP performance level (0.44 m), as detailed by Gutiérrez-Urzúa and Freddi [38]. On the other hand, R-6 aims for a top story drift of 0.385 m (3.2 %), resulting in a design that serves as a testing ground for a less conventional retrofitting design approach with smaller BRBs' cross-sections. This solution exploits a larger portion of the ductility capacity of the MRFs, and, consequently, is expected to be damaged and potentially not repairable after a severe earthquake. The fundamental period of the retrofitted structures is 0.70 s and 0.96 s for R-4 and R-6, which contrasts with the fundamental period of the non-retrofitted structure of 1.88 s. The interested reader can refer to Gutiérrez-Urzúa and Freddi [38] for additional details.

3.2. *Numerical modeling*

The case study structures are numerically modeled in OpenSees. Columns are modeled by considering a distributed plasticity approach to account for flexural-axial interaction. The constitutive behavior of the section fibers is described by the *Steel01* material model in OpenSees, with a kinematic hardening of 0.3 %. Beams are modeled by a concentrated plasticity approach. The plastic hinges at the beam ends are modeled by the *Bilin* material in OpenSees with 1.0 % sectional kinematic hardening, while panel zones are modeled by the *Scissors* model [41]. Further details are provided in Gutiérrez-Urzúa et al. [42]. On the other hand, BRBs are modeled by considering a series arrangement, as shown in Fig. 2. For simplicity, the non-yielding portions of the BRB device and the BRBs connections are represented by the elastic brace element, whereas the BRB device spring concentrates all the plasticity in the BRB model.

Fig. 3 shows the first-mode proportional pushover curve for the two retrofitted structures, including markers at the steps at which the BRBs devices yield at each story and the point at which they reach a ductility of 20 (*i.e.*, as intended in the design). The figure also shows the step at which the MRF exceeds the CP performance level, where collapse is conventionally assumed. In addition, the pushover curve for the bare MRF (*i.e.*, the non-retrofitted structure) is included for comparison purposes. As a result of the design strategy, the different ductility thresholds are exceeded almost simultaneously at all stories. The slight differences are a consequence of the simplifying assumptions made in the design, particularly the bilinearization of the system under an elastic-perfectly plastic capacity curve (thus neglecting hardening).

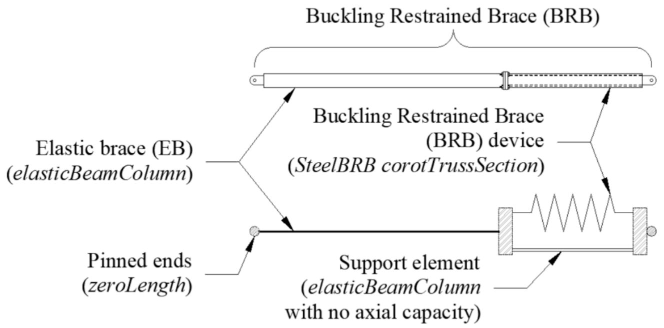

Fig. 2. Modeling approach for the braces, including the BRB device, the elastic brace, and the support element.

4. Ground motion sampling procedures

4.1. *Earthquake hazard*

The case study structures are analyzed under multiple earthquakes following the framework described in Section 2. For this purpose, an earthquake hazard function for the site is obtained from the USGS Unified Hazard Tool [43] by using the Conterminous US database (v4.2.0). In agreement with the retrofitting design, the structure is assumed to be located in Los Angeles and on a soil Class D ($V_{s30} = 259$ m/s). Fig. 4 shows the hazard functions for the site, $\lambda_{IM}(im)$, obtained considering the spectral acceleration at the fundamental period of vibration of the structures as *IM*, *i.e.*, $IM = S_a(T_1)$. The minimum *IM* threshold (im_{min}) considered is 0.05 g, as earthquakes with intensity below this limit do not result in plastic demands on the case study structures and do not contribute to the cumulative strain of the BRBs. Hence, earthquakes with intensity lower than 0.05 g are neglected in the present study.

Fig. 5 shows the Probability Mass Function (PMF) and the Cumulative Distribution Function (CDF) for the site and case study structures, with a design lifespan $t_L = 50$ years, as typically assumed for conventional building structures, and $im_{min} = 0.05$ *g*. As observed, the maximum probability mass value corresponds to $n = 8$ for R-4 and to $n = 6$ for R-6. The number of ground motions per sequence (n_{max}) is established such that $P(N > n_{max}|t_L) < 0.001$, being $n_{max} = 19$ and 15 for R-4 and R-6, respectively. Considering more earthquakes per sequence would have a negligible impact on the results while adding significant computational demands.

4.2. *Ground motion records databases*

A ground motion database of 3,717 accelerograms is assembled from four sources widely used in literature, as follows:

a) 1,794 horizontal ground motion records sourced from the NGA West2 Database [44]. Most of these ground motions were recorded in the West USA Contiguous Coast. A small amount was recorded in Alaska, Armenia, Canada, El Salvador, Georgia, Greece, Iran, Italy, Mexico, Montenegro, New Zealand, Taiwan, and Turkey.
b) 918 horizontal ground motion records sourced from the European Strong Motion Database [45]. These records were sourced from the Mediterranean and Middle East regions.
c) 415 horizontal ground motion records sourced from the Italian Accelerometric Archive [46].
d) 590 horizontal ground motion records sourced from the SIMBAD Database [47]. This database contains shallow crustal ground motions recorded in Japan, Iran, New Zealand, United States, Turkey, Greece, Italy, and other countries in Europe.

Fig. 6 illustrates the records selection, classification, and definition of

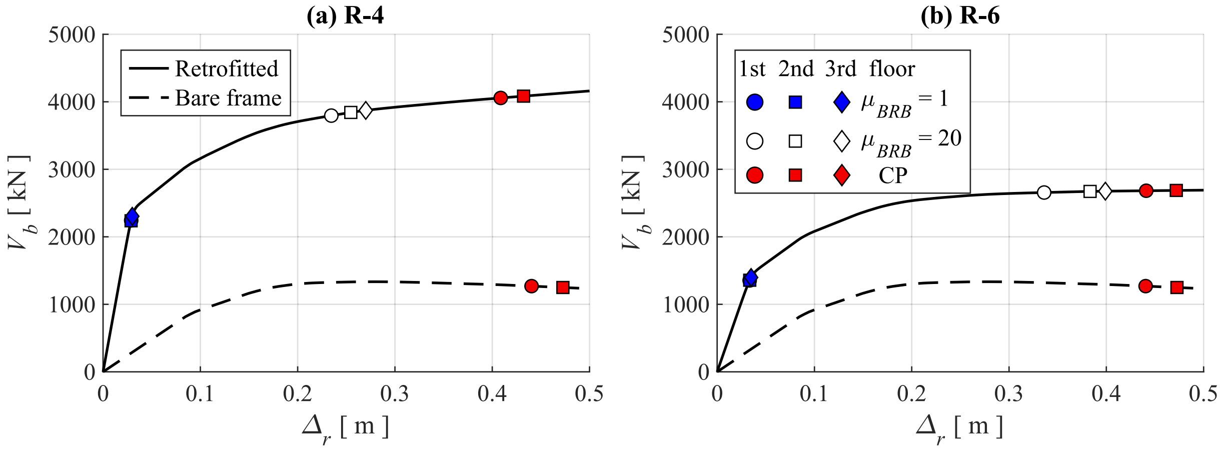

Fig. 3. Pushover curve of the case study structures, including markers at which BRBs devices yield ($\mu_{BRB} = 1$), reach their design ductility ($\mu_{BRB} = 20$, associated to a 975 years return period), as well as markers where the MRF exceeds the CP performance level. The pushover curve of the bare MRF is provided for comparison purposes.

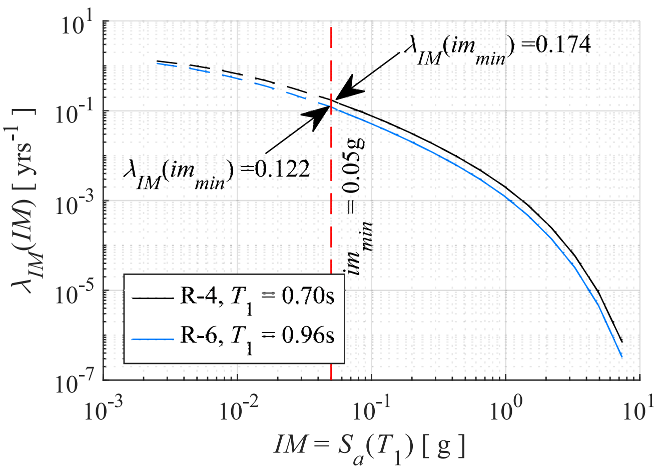

Fig. 4. Hazard function for the site and case study structures for $IM = S_a(T_1)$.

the databases. Each of the considered records in the assembled database is unique. The records are selected (1) to broadly represent the *IM* distribution of the hazard, such that the oversampling of any given record is avoided at any intensity range, and (2) to provide a large sample of pulse-like and non-pulse-like records with high intensities. The 3,717 records database is divided into two more refined groups: Database A, which contains 'strong pulse-like' records, and Database B, which contains 'strong non-pulse-like' records. In addition, both databases contain all the records that are not classified as 'strong'.

The classification of 'strong' and 'pulse-like' records is based on previous studies [48] as follows:

a) A ground motion record is considered 'strong' if it has a Peak Ground Velocity (*PGV*) higher than 0.3 m/s;
b) A ground motion record is considered 'pulse-like' if it has a pulse indicator value i_{pulse} higher than 0.85.

The pulse indicator i_{pulse} is a predictor of the likelihood that a given record is pulse-like [48] and is defined as follows:

$$i_{pulse} = \frac{1}{1 + e^{-23.3+14.6(PGV_{ratio})+20.5(I_{E-ratio})}} \tag{6}$$

in which a i_{pulse} value close to one indicates pulse-like records, while a value close to zero indicates non-pulse-like traits.

The parameters PGV_{ratio} and $I_{E-ratio}$ in Eq. (6), can be obtained by performing a wavelet decomposition of the velocity signal of the ground motion. Following the approach proposed by Baker [48], the decomposition is done by employing a mother Daubechies wavelet of order 4. After the decomposition, the approximation of the wavelet associated with the largest coefficient is calculated and subtracted from the original

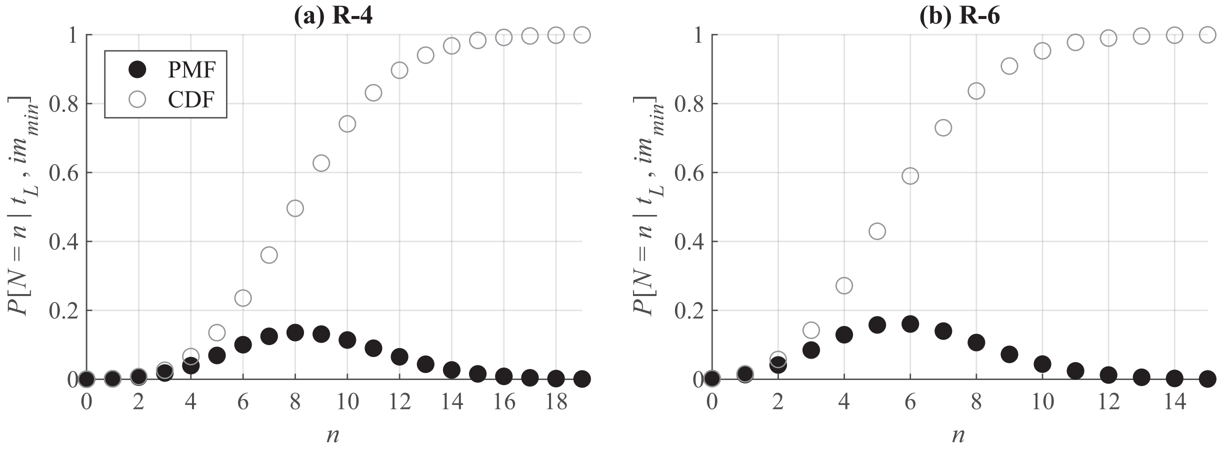

Fig. 5. Probability of $N = n$ earthquakes with im_{min} occurring in a lifespan t_L: Probability Mass Function (PMF) and Cumulative Distribution Function (CDF) for (a) R-4 and (b) R-6.

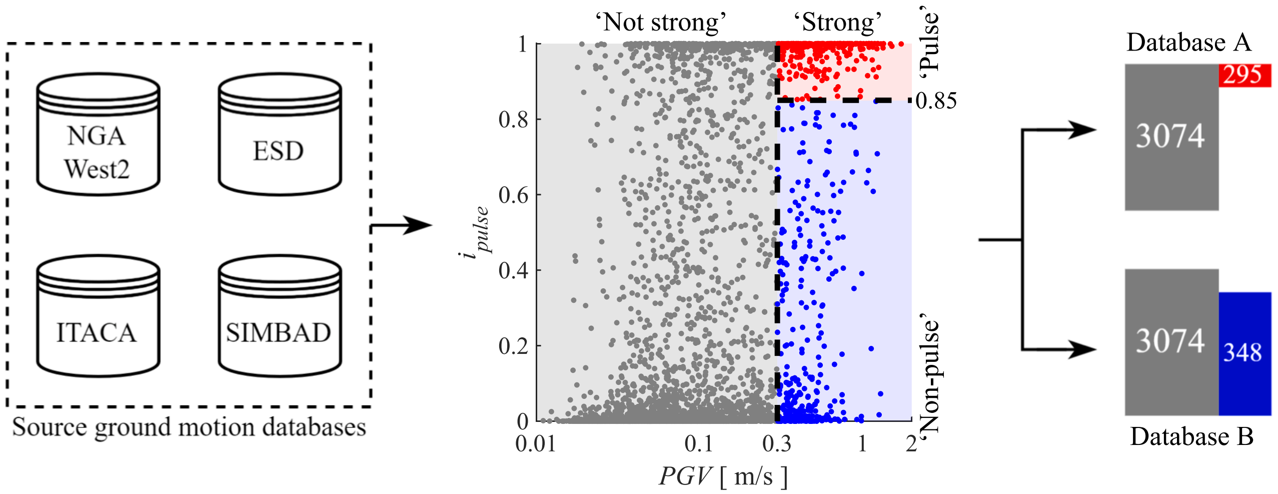

Fig. 6. Graphical representation of the ground motion record classification based on *PGV* and i_{pulse}, along with the assembling of the pulse-like and non-pulse-like record pools.

signal, such that a residual velocity signal is obtained. The comparison between the residual and original velocity signals allows understanding how well a single Daubechies wavelet of order 4 can represent the original signal, *i.e.*, how well the signal is described by a single pulse. This way, the PGV_{ratio} is the ratio between the *PGV* of the residual and original velocity signals, while $I_{E-ratio}$ is the ratio between the energy contained in the residual and original velocity signals. The energy in the velocity signal is measured by the integral of the ground velocity (also referred to as energy integral) [49,50] as follows:

$$I_E = \int_0^{t_{end}} v^2(t)dt \tag{7}$$

where t_{end} represents the duration of the ground motion record and $v(t)$ is the velocity history. Fig. 7(a) and (b) illustrate examples of pulse- and non-pulse like records, respectively.

After ground motions with 'strong' and 'pulse-like' characteristics are identified they are separated as illustrated in Fig. 6, Database A contains 3,074 'not strong' records, plus 295 'strong pulse-like' records, while Database B contains the same 3,074 'not strong' records, plus 348

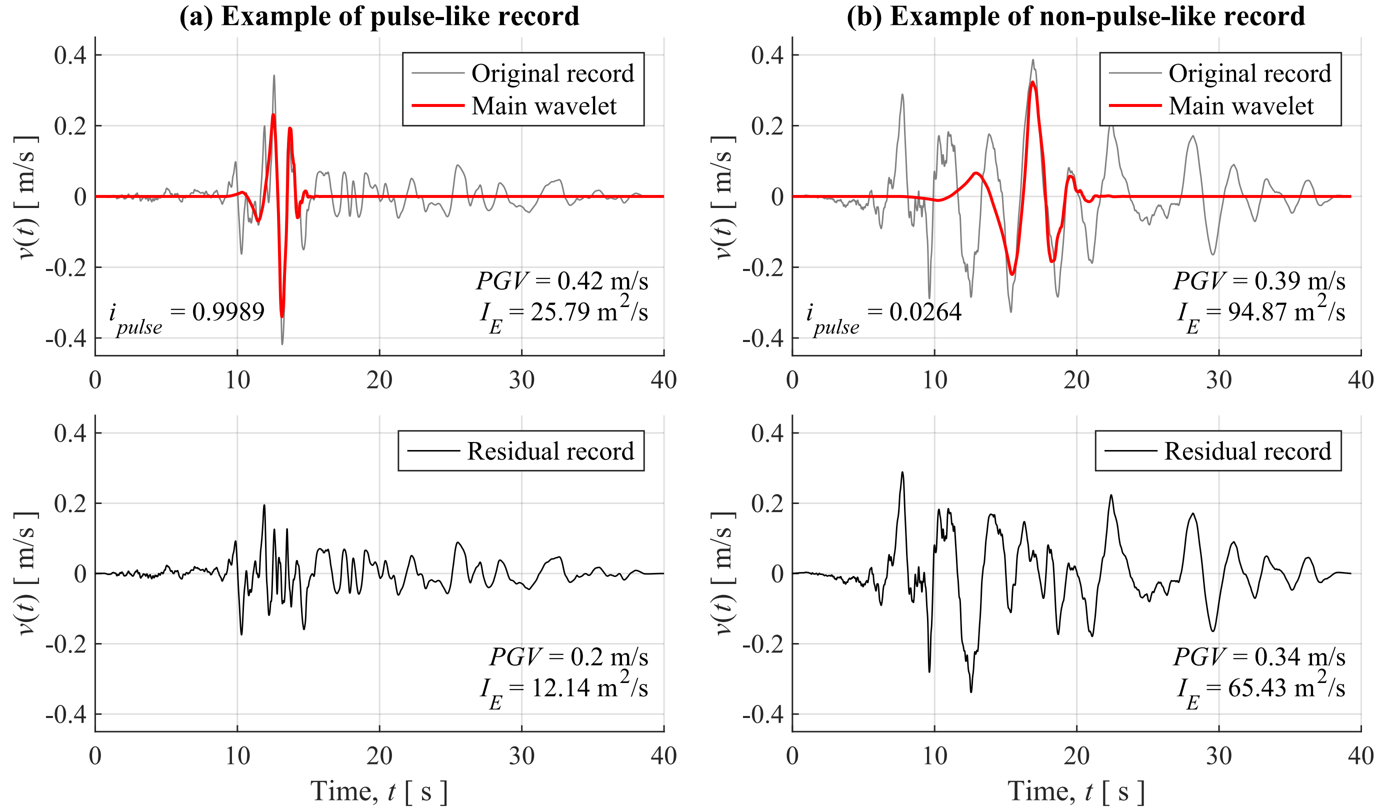

Fig. 7. Examples of velocity signals, wavelet corresponding to their maximum coefficient, and residual signals for (a) pulse-like and (b) non-pulse-like ground motions. Both signals recorded during the 1989 Loma Prieta Earthquake.

‘strong non-pulse-like’ records.

4.3. Ground motion model and sampling

An *IM* matrix **IM** is assembled by considering $n_{seq} = 2{,}000$ sequences of n_{max} earthquakes for each case-study structure. The *j*-th row and *k*-th column of the matrix (for $j = 1, 2, \ldots, n_{max}$ and $k = 1, 2, \ldots, n_{seq}$) is populated with a target intensity measure im_{jk} randomly sampled from the *IM* distribution. Each im_{jk} value in **IM** is matched with one of the ground motion records contained in the source database (either Database A or B). Only those ground motion records in the vicinity of im_{jk} are considered for the random selection. Specifically, only those records with an *IM* in the range from 80 % to 125 % of im_{jk} are considered, such that the scaling factors to match im_{jk} remain close to one. In a few cases (less than 0.07 % of samples in **IM**), the scaling range is extended to include at least 10 ground motions in the sampling pool and ensure that excessive repetition is avoided, which occurs particularly at high *IM* values. According to previous studies, *e.g.*, [51,52], scaling factors up to 4 result in non-significant bias and are acceptable for engineering purposes; thus, this scaling factor is selected as the upper limit for all cases.

In addition, the selection process avoids the repetition of a ground motion record within the same sequence *k*. The polarity of the ground motions utilized in each analysis is also randomized to avoid inheriting the polarity bias from the ground motion database. As previous studies [53,54] have demonstrated that BRBs generally exhibit non-stiffness-degrading responses under seismic events, the modal properties of the structure are not expected to change even after strong earthquakes. Therefore, no additional considerations are required in the definition of *IM* samples for the structures as the fundamental period of the structures remains constant.

5. Demands under multiple earthquakes

As previously discussed, the present study deals with failure modes which occurrence is dependent on the pre-existing state of the structure (*i.e.,* based on state-dependency or cumulative quantities). Hence, the present study uses a multiple earthquake scenarios approach to explicitly track the state-dependent and cumulative effects on the demands. The following three failure modes are investigated:

a) The low-cycle fatigue rupture of BRBs. This is indirectly measured through the number and amplitudes of strain cycles applied on a given BRB. These cycles are measured by employing a rainflow counting algorithm, which simultaneously registers amplitude and number of cycles on that amplitude. This is a cumulative quantity, and the characteristics of previous earthquakes are relevant to the performance of the structure under the following ones.
b) The residual deformation of the dual MR-BRBFs. This is a state-dependent and potentially cumulative quantity as the residual drift observed after an earthquake can be increased or reduced in the following earthquake, depending on the polarity of the ground motion. Excessive residual drifts can result from a single ground motion, or from the cumulative demands from two or more earthquakes. It is also noteworthy that although there is a correlation between peak and residual quantities (*i.e.,* strong ground motions will likely lead to significant demands on both), the residual demands are not solely dependent on the peak quantities, as the ground motion may contain more than one peak with different polarities.
c) The peak demands (ductility demand in BRB and inter-story drift). These are state-dependent quantities as they are affected by the evolution of the structural properties (*e.g.,* isotropic hardening in the BRBs) and the residual demands from previous earthquakes. For example, the peak demands during a strong earthquake can be close to the capacity limit, without exceeding it. However, if the same ground motion is applied on a building with residual deformations, the capacity limits may be now exceeded.

As detailed in the previous sections, each model is analyzed in OpenSees [35] by considering a total of $n_{seq} = 2{,}000$ sequences of ground motions drawn from two different pools of records. Each sequence contains n_{max} sequential ground motions, such that the starting conditions of the structure (*i.e.*, internal forces and deformations) at earthquake *j* correspond to the residual conditions of the structure at earthquake$j - 1$. A large number of zeros acceleration points (*i.e.,* 40 s) have been added at the end of each record to allow the free vibrations to stop and correctly capture the residual displacements.

5.1. EDPs evolution in a single ground motion sequence

To better explain the procedures, Fig. 8 shows the key results for one BRB devices at the 1st story of structure R-4 under the first five shocks of a ground motion sequence. The figure includes the ground acceleration history, $a_g(t)$, the ductility demand history $\mu(t)$, the peak ductility demand history $\mu_p(t)$, and the cumulative plastic ductility demand history $\mu_c(t)$ of the BRB device. The ductility history is simply defined as the axial deformation history of the device at a given time normalized by its yielding deformation, while the peak ductility demand history $\mu_p(t)$ is the maximum absolute peak ductility demand that the BRB has experienced in any previous instant and earthquake. Finally, the cumulative plastic ductility demand $\mu_c(t)$ is defined as the absolute sum of the plastic axial deformation imposed on the BRB, normalized by its yielding deformation. Although $\mu_c(t)$ is not directly comparable to the capacity models presented later in this paper, it is a proxy for the cumulative demands imposed on the devices and is here presented to facilitate the comparison with other ductility-based EDPs.

In the specific sequence illustrated in Fig. 8, the peak ductility demand history $\mu_p(t)$ reaches the value of 5.1 during ground motion 1, remains steady during ground motions 2 and 3, and increases again to 14.2 during ground motion 4. Similarly, the cumulative plastic ductility demand $\mu_c(t)$ increases up to 119.3 after four earthquakes. Ground motions 3 and 5 do not induce an increase as the device remains within its elastic range in those earthquakes. In addition, residual ductility demand $\mu_r(n)$, defined as the residual axial deformation in the BRB normalized by its yielding deformation, is evaluated after each earthquake. In this specific sequence, only ground motion 4 induces a significant residual ductility demand of 2.8.

5.2. EDPs statistics from the $\boldsymbol{n_{seq}}$ sequences

Fig. 9 shows the statistics of the key ductility-related EDPs for the BRBs *vs.* the number of ground motions *n* for all sequences and both case study structures R-4 and R-6. These parameters are obtained by following the approach illustrated in Fig. 8, but presented as a function of the number of ground motions *n*, rather than analysis time *t*. All the EDPs are considered as the maximum in the demand history of any BRB in the structure, meaning that the demands at earthquake *j* reflect not only the demands observed in that earthquake, but the maximum demands observed at any point from earthquake 1 until earthquake *j*.

Fig. 9(a) and (b) show the results for the peak ductility demand $\mu_p(n)$. In both structures, the median $\mu_p(n)$ increases with *n* along with the dispersion, described through the interquartile (25–75 %) and interdecile (10–90 %) ranges. It is worth noting that the median values are almost identical regardless of the type of ground motions considered (*i.e.,* pulse-like or non-pulse-like). Conversely, the dispersion increases with *n* when considering the pulse-like pool. This arises from the algorithm used to define ground motion pools, where the majority of records are common to both pools, and only the ‘strongest’ records are discriminated. Unlike the median, the mean values do exhibit a clear tendency to increase when pulse-like records are considered, as a

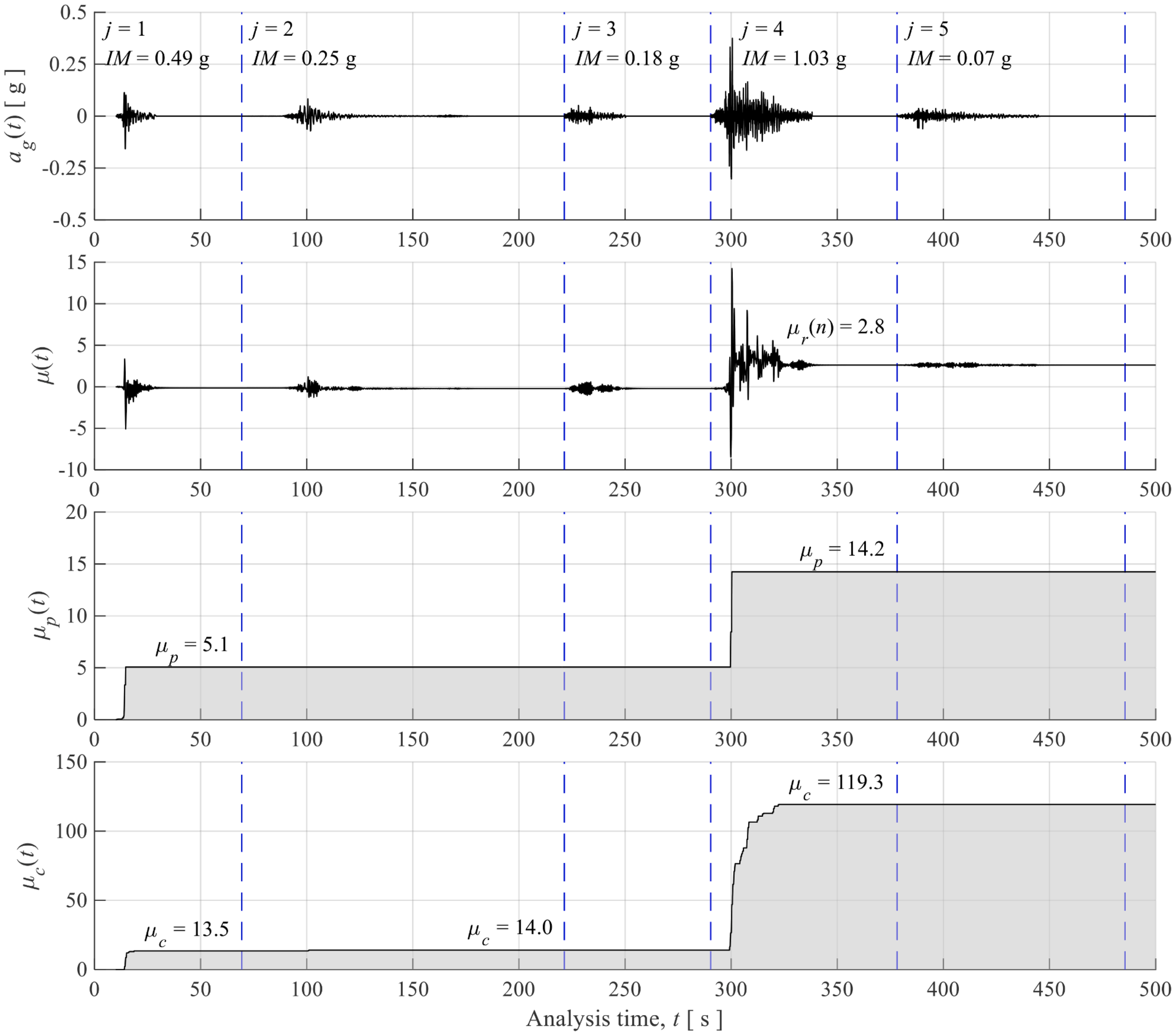

Fig. 8. EDPs evolution in a single ground motion sequence.

consequence of longer tails on the right side (*i.e.*, higher values) of the distribution.

Fig. 9(c) and (d) show the results for the residual ductility demand $\mu_r(n)$. As in the case of $\mu_p(n)$, the median quantities are similar among the pulse-like and non-pulse-like pools, the dispersion is larger for the pulse-like pool. Moreover, this EDP is characterized by a larger dispersion than the peak quantities analyzed in Fig. 9(a) and (b). This is also reflected in the mean values, which lie on or above the third quartile of the distribution.

Fig. 9(e) and (f) show the results for the cumulative plastic ductility demand $\mu_c(n)$. Unlike the peak and residual quantities, both the mean and the median cumulative plastic ductility demand $\mu_c(n)$ imposed on the BRBs are larger when considering non-pulse-like ground motions. This difference is explained by the larger number of cycles that are typically observed in a record classified as non-pulse-like, compared to a pulse-like record with the same $IM = S_a(T_1)$.

6. Capacity models

The samples of the demand recorded during the sequential analyses are compared to corresponding capacity values at the end of each earthquake in the sequence, such that the condition $(D_i > C_i | N = n)$ is evaluated as in Eq. (1). The suffix i represents the i-th failure mode. The considered failure modes are:

a) Failure of the BRB due to low-cycle fatigue after repeated cycles of plastic strain on the steel core.
b) Failure of the BRB due to peak ductility demand. This is related to the design and qualification ductility values considered for each BRB device.
c) Residual deformations imposed on the structure as a proxy of its repairability. Residual quantities are compared in terms of a global EDP (*i.e.*, residual inter-story drift ratio) considering the repairability limits in literature, which synthesize both structural and non-structural aspects.
d) Failure of the MRF components. The peak inter-story drift ratio of the structure is used as a proxy of the structural damage imposed on the MRF elements, including beams, columns, and panel zones.

A summary of the considered EDPs and their corresponding capacity values is provided in Table 2. The following subsections elaborates on the capacity values and models for the different EDPs.

6.1. Capacity models for low-cycle fatigue

Several models have been developed to predict the cumulative

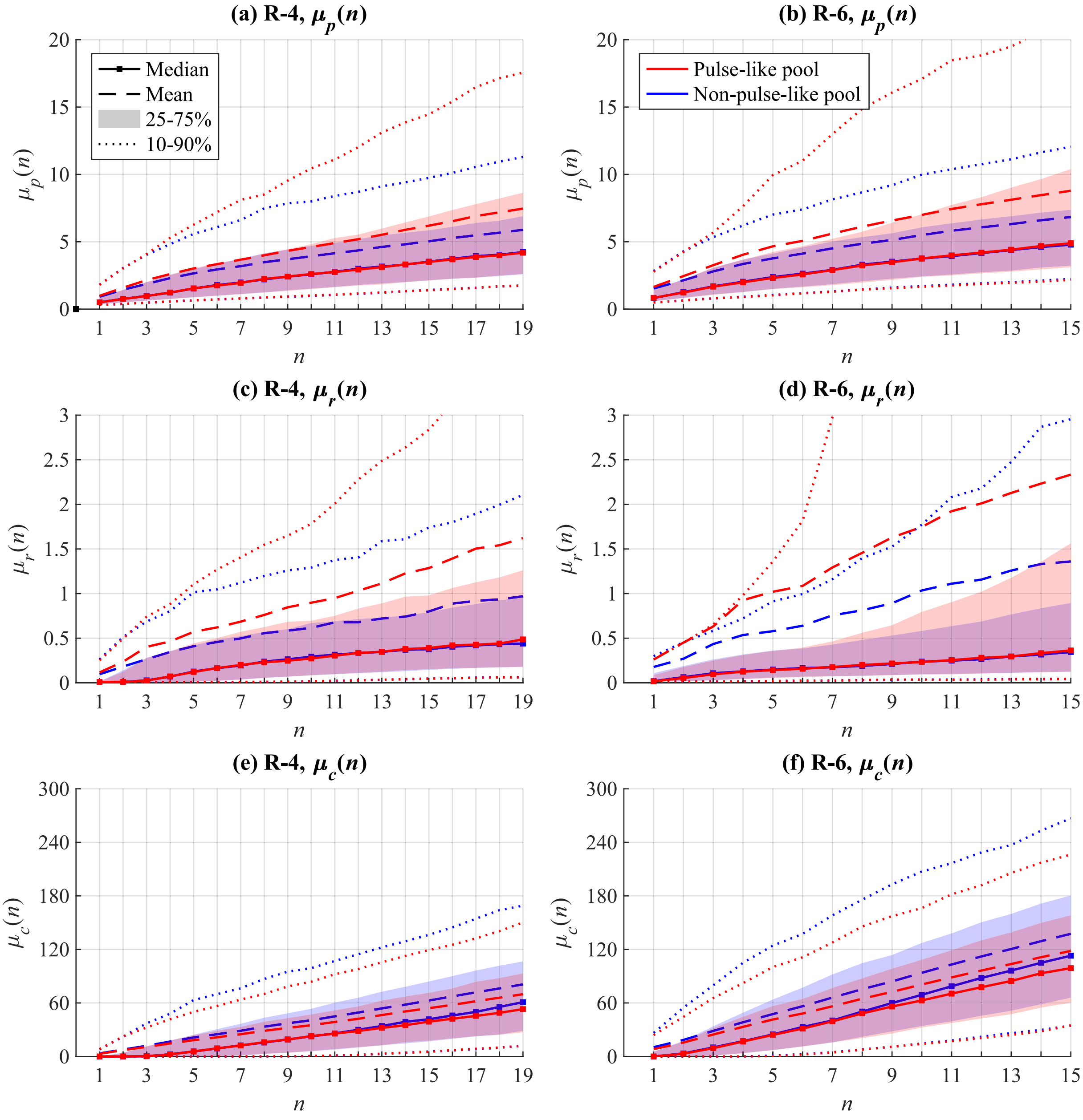

Fig. 9. EDPs statistics from the n_{seq} sequences for: peak ductility demand $\mu_p(n)$ for (a) R-4 and (b) R-6; residual ductility demand $\mu_r(n)$ for (c) R-4 and (d) R-6; and cumulative plastic ductility demand $\mu_c(n)$ for (e) R-4 and (f) R-6.

ductility demand required to reach low-cycle fatigue failure. Most of these models are based on the Coffin-Manson relationship [23,24], as the most common approach to describe the fatigue life of metallic elements in other industries (such as mechanical or aerospace engineering). The Coffin-Manson relationship for a given metallic element can be built through the monotonic cyclic testing of multiple samples, each of which is tested with a constant-amplitude protocol until failure. The amplitude of the strain cycles ($\Delta\varepsilon_t$) on each tested specimen is plotted against the number of cycles required to reach low-cycle fatigue (N_f), such that a model can be fitted according to the following form:

$$\ln(N_f) = \beta_1 + \beta_2 \ln(\Delta\varepsilon_t) \pm \eta \tag{8}$$

in which β_1 and β_2 are regression coefficients, and η represents a zero-mean error term describing lack of fit. Although this model is developed by considering constant-amplitude loading protocols, it can be applied to a random time-history through the Miner's rule, which is expressed as follows:

$$MDI = \sum_{j=1}^{N_{full}} \frac{1}{(N_f)_j} + \frac{1}{2} \sum_{k=1}^{N_{half}} \frac{1}{(N_f)_k} \tag{9}$$

where N_{full} and N_{half} represent the number of full and half strain cycles for each strain cycle amplitude ($\Delta\varepsilon_t$), respectively. N_f is obtained from Eq. (8) for each cycle amplitude $\Delta\varepsilon_t$. The Miner's Damage Index (MDI) represents the proportion of the fatigue capacity utilized in the BRB core, such that $MDI = 1$ denotes the low-cycle fatigue rupture. In order to define the number and amplitude of full and half strain cycles, the rainflow counting algorithm [55] is used. An example of application of the rainflow counting algorithm is presented in Fig. 10. In this example, three half cycles are counted: $\Delta\varepsilon_t = 0.01$ in tension (magenta), $\Delta\varepsilon_t = 0.02$ in compression (blue), and $\Delta\varepsilon_t = 0.04$ in tension (red); along with two full cycles: $\Delta\varepsilon_t = 0.02$ (green) and $\Delta\varepsilon_t = 0.01$ (yellow). For each $\Delta\varepsilon_t$ value, a corresponding N_f value is obtained by sampling the function

Table 2
Summary of considered EDPs and corresponding capacity values.

EDP,D_i	**Capacity value,**C_i	**Description**
Number of cycles $N_f(\Delta\varepsilon_t)$, counted through the Miner's Damage Index *MDI*	Miner's Damage Index for all fatigue models $MDI_{All} = 1$	Low-cycle fatigue rupture of BRB core in any of the capacity models
	Miner's Damage Index for Li et al. [18] model $MDI_{Li} = 1$	Low-cycle fatigue rupture of BRB core in the Li et al. [18] capacity model
Peak ductility demand μ_p	$\mu_{p1} = 20$	Design ductility
	$\mu_{p2} = 40$	Qualification ductility
Residual inter-story drift ratio IDR_r	$IDR_{r1} = 0.2$ %	Repairs and adjustments to non-structural elements required
	$IDR_{r2} = 0.5$ %	Recentering required, or not feasible to repair
Peak inter-story drift ratio IDR_p	IDR_{IO}	MRF elements exceed the IO
	IDR_{CP}	MRF elements exceed the CP

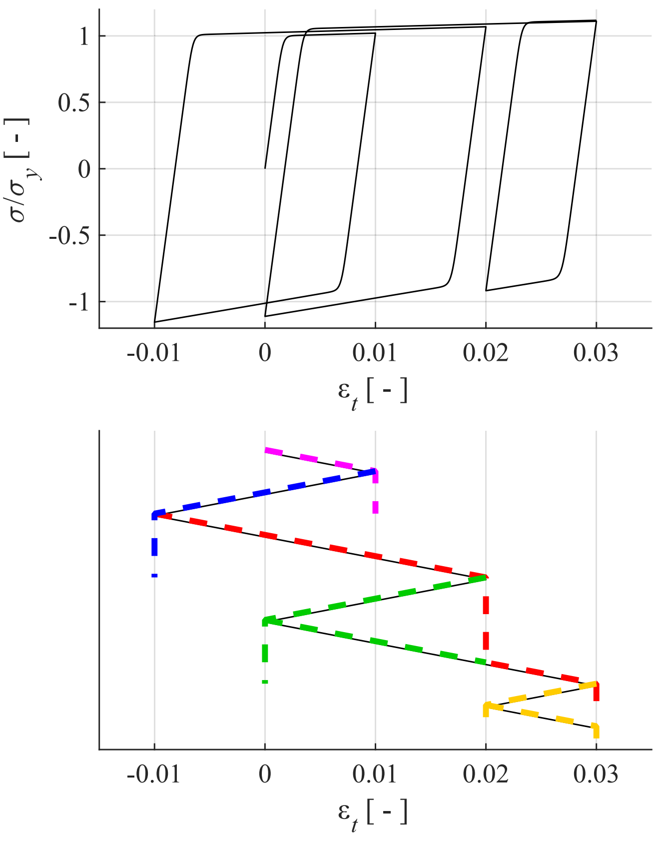

Fig. 10. A graphical example of the rainflow counting algorithm.

corresponding to the chosen Coffin-Manson model. Table 3 present six low-cycle fatigue models based on the Coffin-Manson relationship of Eq. (8).

The main low-cycle fatigue model considered in this study is the one proposed by Li et al. [18]. This model was developed based on tests of BRBs made with a steel-core plate in a mortar-filled tube and with core and sleeve materials matching those considered in the present study. Moreover, the model provided by Li et al. [18] includes information on the model accuracy (*i.e.*, the error term in Eq. (8)). The capacity limit related to this model is herein referred to as MDI_{Li}.

Other low-cycle fatigue models were considered. These models include Chen et al. [21], Xie et al. [19], Takeuchi et al. [20] models and two of the models used by Tong et al. [56], referred to as Huang and Shi JianHua models. The first two models were calibrated based on experiments performed on all-steel BRBs and Chinese material properties. Takeuchi et al. [20] model was calibrated on BRBs composed of plate or cross-core elements confined by a mortar-filled tube, assembled with Japanese steel standards. No details are provided on the BRB composition or materials considered to calibrate the Huang and Shi JianHua models, yet these are included as they represent the lowest capacity models found in the literature, particularly at large amplitude strain cycles. Fig. 11 shows a comparison of the considered models *i.e.*, the relationship between the number of cycles required to reach low-cycle fatigue (N_f) and the amplitude of the strain cycles ($\Delta\varepsilon_t$). Given the uncertainty in the model selection, a second capacity limit is established by conservatively assuming the envelop from all these low-cycle fatigue models, and referred to as MDI_{All}, *i.e.*, if the low-cycle fatigue capacity is exceeded in any of the models, it is considered that $MDI_{All} > 1$.

6.2. *Capacity limits for residual EDPs*

As a consequence of their low post-yielding stiffness, the use of BRBs can result in large residual drifts in the structure after a strong earthquake [9,25] residual inter-story drift demands are monitored after each earthquake.

Two residual capacity limits are considered: $IDR_{r1} = 0.2$ % to describe the limit at which adjustment and repairs are needed to non-structural and mechanical components (FEMA P-58-1 [30]); and $IDR_{r2} = 0.5$ % to describe cases where structural repair may not be economically convenient [26,27] or the realignment of structural frame and related structural repairs may be required to maintain permissible drift limits for non-structural and mechanical components and to limit degradation in structural stability (FEMA P-58-1 [30]). Regardless of the physical interpretation of $IDR_r > IDR_{r2}$, the BRB devices can be considered as failed, as the structure will be either in the need of demolition or in the need of realignment.

6.3. *Capacity limits for peak EDPs*

The present study considers two peak EDPs as indicators of structural damage. The first one is related to the peak ductility in the BRBs, for which two capacity limits are established: $\mu_{p1} = 20$, associated with the design ductility of the BRBs, as considered by the designers [38]; and $\mu_{p2} = 40$ (*i.e.*, twice the design ductility), associated with the peak ductility required in the loading protocol used for qualification in the AISC 341 [15]. Although the latter does not necessarily correspond to the actual rupture of the BRB device, a ductility demand beyond the qualification limits is likely to result in the replacement of the device.

The second one is the peak inter-story drift ratio. This EDP is intended to monitor the deformation capacity of the MRF elements. For this purpose, the inter-story drift ratio is mapped through a pushover analysis, such that the capacity limits are established as the inter-story drift ratios at which any element exceeds its acceptance criteria. These are defined based on the ASCE 41–17 [39] capacity values for beams, columns, and panel zones. Two global performance levels are considered: the inter-story drift ratio at which any MRF element reaches the IO performance level, IDR_{IO}; and the CP performance level, IDR_{CP}. These inter-story drift values are different for each story and case-study structure. For the R-4 they correspond to 0.83, 1.14 and 1.92 % at IO performance level, and 3.38, 3.91 and 5.00 % at CP performance level for the first, second, and third floors, respectively. For the R-6 they correspond to 0.82, 1.15 and 2.10 % at IO performance level, and 3.65, 4.25 and 5.00 % at CP performance level for the first, second, and third floors, respectively.

Table 3
Parameters and characteristics of the low-cycle fatigue models.

Model	β_1	β_2	η	Core material	BRB type
Li et al. [18][1]	−4.1942	−2.2695	0.1904 t_2	ASTM A36	Plate in mortar-filled tube
Chen et al. [21]	−1.3315	−1.4025	–	Q235B	All-steel
Xie et al. [19]	−3.8678	−2.1322	–	Q235	All-steel
Takeuchi et al. [20][2]	−37.8451	−7.1429	–	LY100, SN400B, LY225, SS400	Plate or cross in mortar-filled tube
	−3.2362–0.8679	−2.0408–1.4085			
Huang [3]	−3.9686	−1.9305	–	–	–
Shi JianHua [3]	−0.0036	−2.2573	–	–	–

Note: [1] The variable 't_2' represents a random value in a Student's t distribution with 2 degrees of freedom; [2] The Takeuchi et al. [20] model is divided into three segments; [3] The Huang and Shi JianHua models were retrieved from Tong et al. [56].

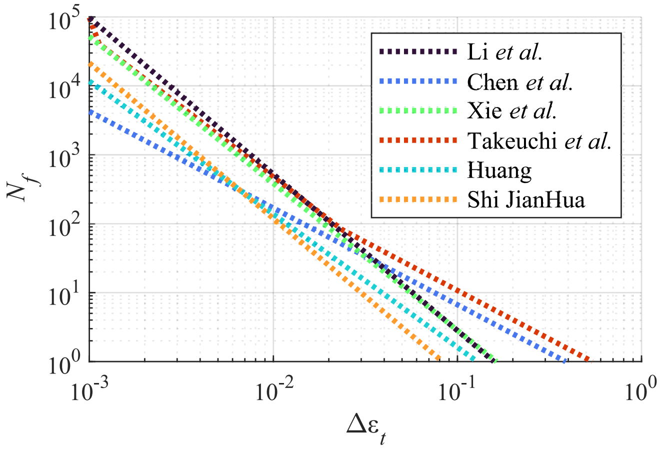

Fig. 11. Graphical comparison of the low-cycle fatigue models.

7. Risk assessment

The risk of a given failure mode to occur, *i.e.*, $P(D_i > C_i|t_L)$, as defined in Eq. (1), is evaluated in this section through a Monte-Carlo approach. The EDPs obtained from the $n_{seq} = 2{,}000$ demand sequences are contrasted to corresponding capacity values. In the case of the Li et al. [18] low-cycle fatigue model, which is accompanied by an error term, a total of $n_{sam} = 25$ randomly sampled capacity values are considered for each BRB and contrasted to each EDP sequence, while the rest of the capacity values are considered in a deterministic manner.

7.1. Risk when considering independent failure modes

Fig. 12 shows the evolution of the probability of each failure model as a function of the number of earthquakes n. The risk values related to peak and residual EDPs are historically cumulative, which means that once a capacity limit is exceeded at earthquake j, the capacity limit is considered as exceeded for the rest of the sequence. The low-cycle fatigue is cumulative by nature, thus the cumulative demands are the sum of the demand history observed in all previous earthquakes. The current section considers the failure modes independently from each other. Based on Fig. 12, several observations can be made:

- **Residual drifts.** The probability of exceeding the capacity limits associated with the residual drifts is very significant in both structures, and particularly in the case of pulse-like ground motions. The IDR_{r1} limit, associated with the need for repairs and alignments on non-structural components, is almost as probable as IDR_{IO}, limit above which the structural components may also require some light intervention. The IDR_{r2} limit, associated with the need of recentering the structure, is particularly sensitive to the pulse-like ground motions, as the probability is tripled for R-4 and doubled for R-6, compared to the non-pulse-like earthquakes case. This failure mode is the most relevant for the assessment of the case study structures, as it is the most likely to occur among those that result in the loss of the structure, either due to high repair cost or to be considered as collapsed (*i.e.*, IDR_{CP}, μ_{p2}).
- **Low-cycle fatigue.** The probability of exceeding the capacity to low-cycle fatigue is very low in all cases, being higher in R-6 in comparison to R-4. This suggest that, despite both buildings being designed for the same hazard and ductility, the design approach that allows a larger BRB deformation results in larger cumulative strain demands. When considering the Li et al. [18] model alone, the probability of exceeding the capacity is practically negligible, as the model attributes a very large fatigue capacity to the devices. Nonetheless, even when considering failure according to any of the models in Table 3, the probability of low-cycle fatigue rupture is very low in both structures. The differences between pulse- and non-pulse-like sets are negligible. This may be attributed to the fact that both ground motion pools share the same non–'strong' records, which represent the vast majority of the sampled earthquakes according to the considered site hazard.
- **Peak ductility.** The probability of exceeding the μ_{p1} capacity limit, associated with the design peak ductility of the BRBs, is significantly larger when considering pulse-like ground motions. It is also slightly larger when considering R-6 case study structure for the same number of earthquakes, which is expected as this case study structure was designed for a larger deformation allowance. The probability of exceeding the capacity limit associated with the qualification ductility, μ_{p2}, is practically negligible (with the exception of R-6 in pulse-like scenario), particularly when compared to the capacity limits associated to residual deformation.
- **Peak demands on MRF elements.** In general, for both case study structures and ground motion pools, the exceedance of IDR_{IO} is the failure mode with the largest probability of occurrence for all the number of earthquakes. This is expected as the capacity limits for IO are much stricter than those for CP and those employed for other failure modes. In contrast, the probability of exceeding IDR_{CP} is negligible in R-4, and low in R-6 when considering non-pulse-like records. It is non-negligible only for pulse-like records and R-6.

With the exception of low-cycle fatigue in R-4, the probability of exceeding a capacity value grows roughly linearly with respect to the number of earthquakes n. This is likely a result of the BRBs initial stiffness, which does not degrade after a ground motion, hence keeping the modal properties of the structure almost unaltered; hence, it cannot be generalized for other lateral resisting frame types (*e.g.*, MRFs). The low-cycle fatigue in R-4 could be better described by a bilinear relationship in which the lower n values remain asymptotic to zero, followed by a roughly linear increase after a given number of earthquakes which depends on the ground motion characteristics (*e.g.*, pulse *vs.* non-pulse).

Although the comparison in terms of the number of earthquakes n allows understanding which failure modes are more likely to occur and

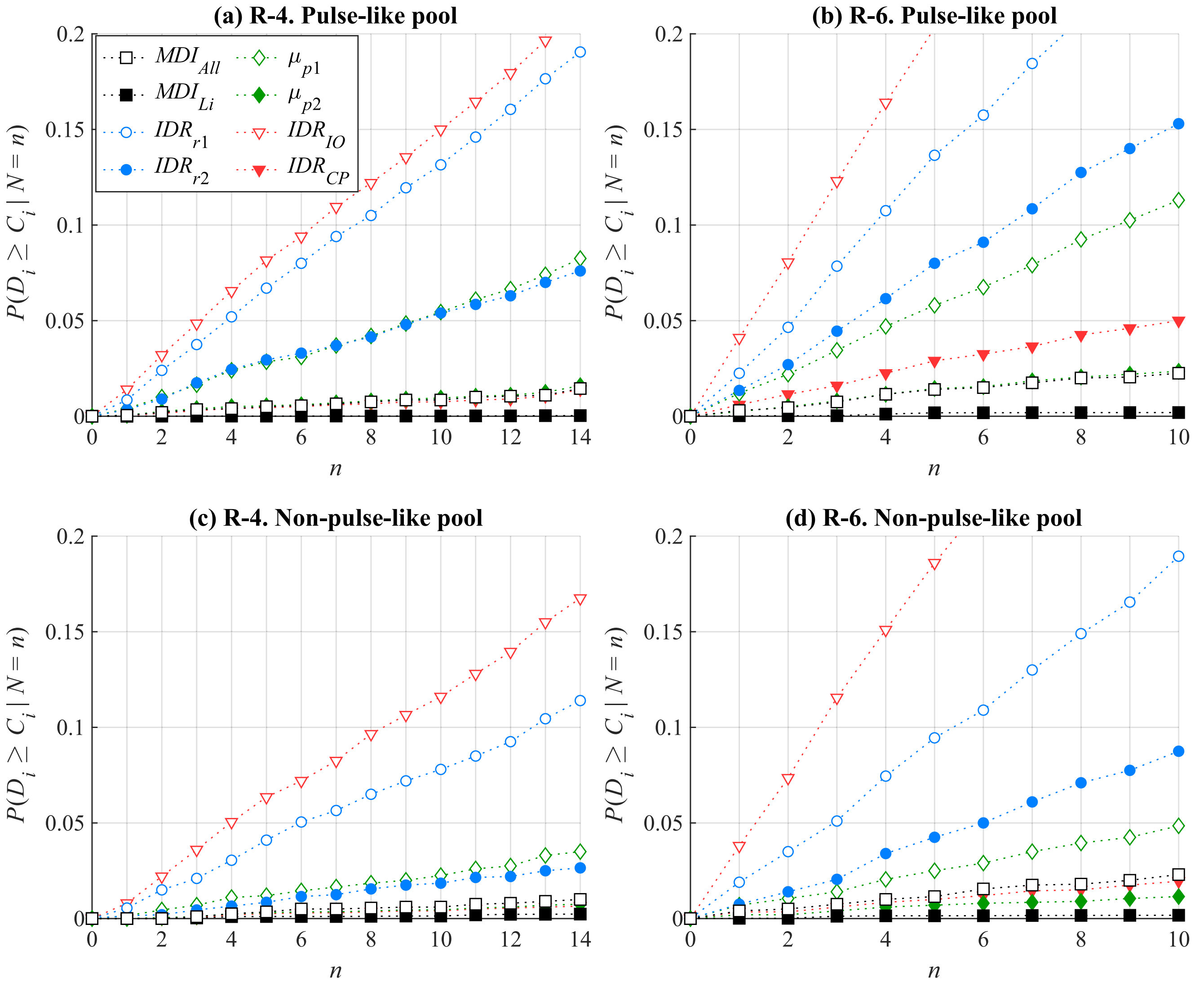

Fig. 12. Probability of failure given n for all considered failure modes for (a) pulse-like and (c) non-pulse-like ground motions in R-4, (b) pulse-like and (d) non-pulse-like ground motions in R-6.

their evolution with respect to the ground motions number, it does not allow a fair comparison between case study buildings in terms of risk. Thus, the probabilities of exceeding a capacity value given $N = n$ is combined with the probability of having $N = n$ earthquakes in t_L years, as established in Eq. (1), to obtain risk estimates conditional to t_L. Fig. 13 shows a summary of the risk values associated with each capacity limit when considering a time frame $t_L = 50$ years, intended to represent the design lifetime of an average structure.

As observed, the risk values for the BRBs' low-cycle fatigue rupture are very low, for both pulse-like and non-pulse-like ground motion pools. Although MDI_{All} represents an envelope for a variety of BRB low-cycle fatigue models, its associated risk values still result negligible when compared to the risk of excessive residual deformation.

The risk of exceeding the residual capacity limits IDR_{r1} and IDR_{r2}, associated with minor reparations and realignment of the structure, respectively, is significantly larger when considering pulse-like ground motions regardless of the case study structure. For IDR_{r2}, the risk values are approximately doubled in both case study structures. Thus, the consideration of pulse-like or non-pulse-like ground motions has a large impact on the residual deformations observed in the case study structures.

Similar results are also observed for the risk of exceedance of the peak ductility capacity limits, μ_{p1} and μ_{p2}, as well as of IDR_{CP}, the values of which are approximately doubled for pulse-like ground motions compared to non-pulse-like motions. This is not the case for the risk of exceeding IDR_{IO}, which is similar for both pools of ground motions, hence suggesting that the characteristics of the ground motion have a limited impact on the occurrence of the low damage levels associated with the IO performance.

Finally, even though the two retrofit schemes have been designed considering the same hazard model and ductility, the R-4 case study structure exhibits lower values of risk for all capacity limits, with respect to R-6. Hence, designing for a larger deformation target will not only impact the drift-related capacity limits, but also the low-cycle fatigue ones.

7.2. *Risk when considering mutually exclusive failure modes*

In the previous section, the risks are evaluated independently for the various failure modes. This implies that two or more failure modes could be exceeded within n earthquakes, and a failure mode could occur during earthquake j ($j = 1,2,\ldots,n_{max}$) even if a different failure mode

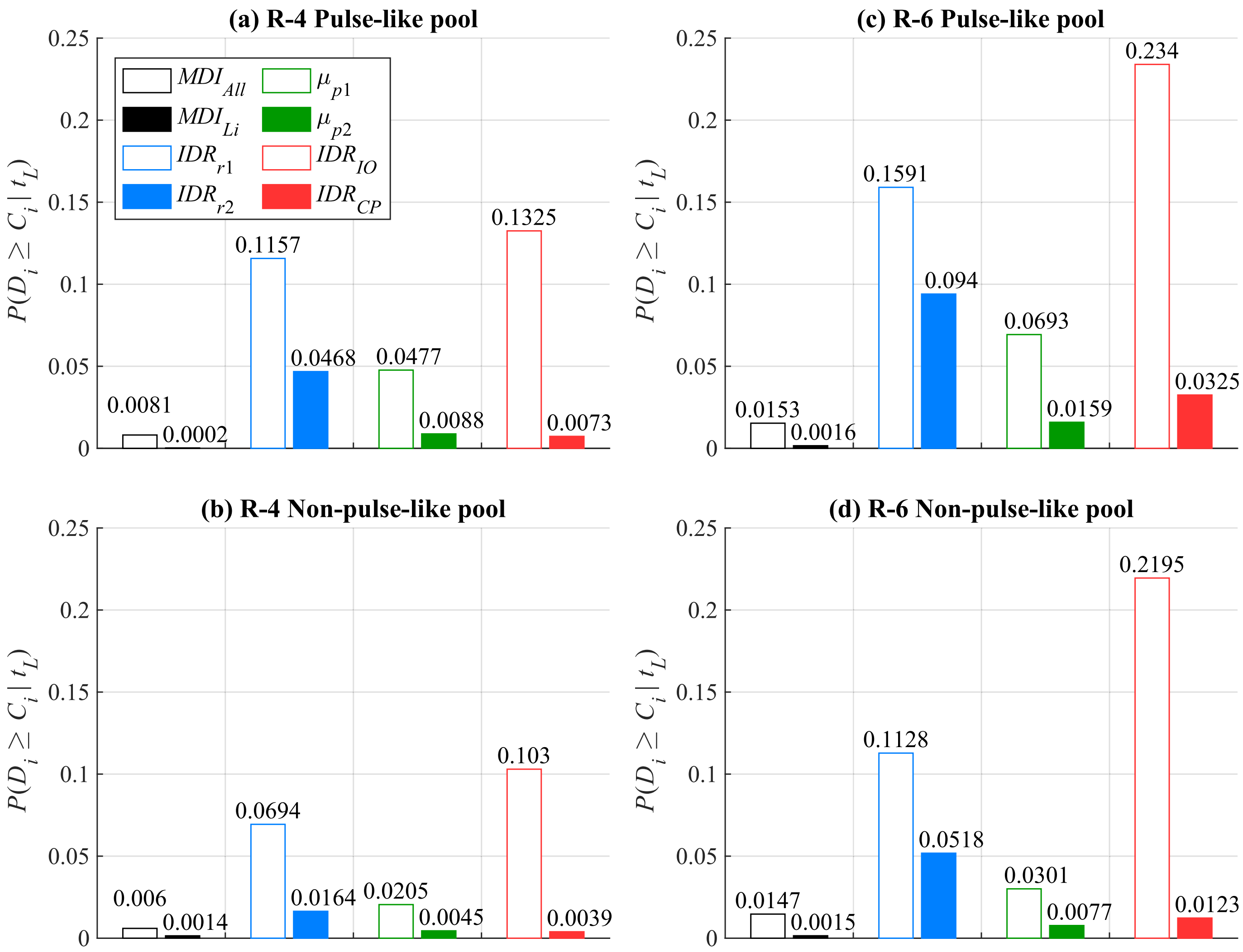

Fig. 13. Probability of failure given t_L for all considered failure modes for (a) pulse-like and (c) non-pulse-like ground motions in R-4, (b) pulse-like and (d) non-pulse-like ground motions in R-6.

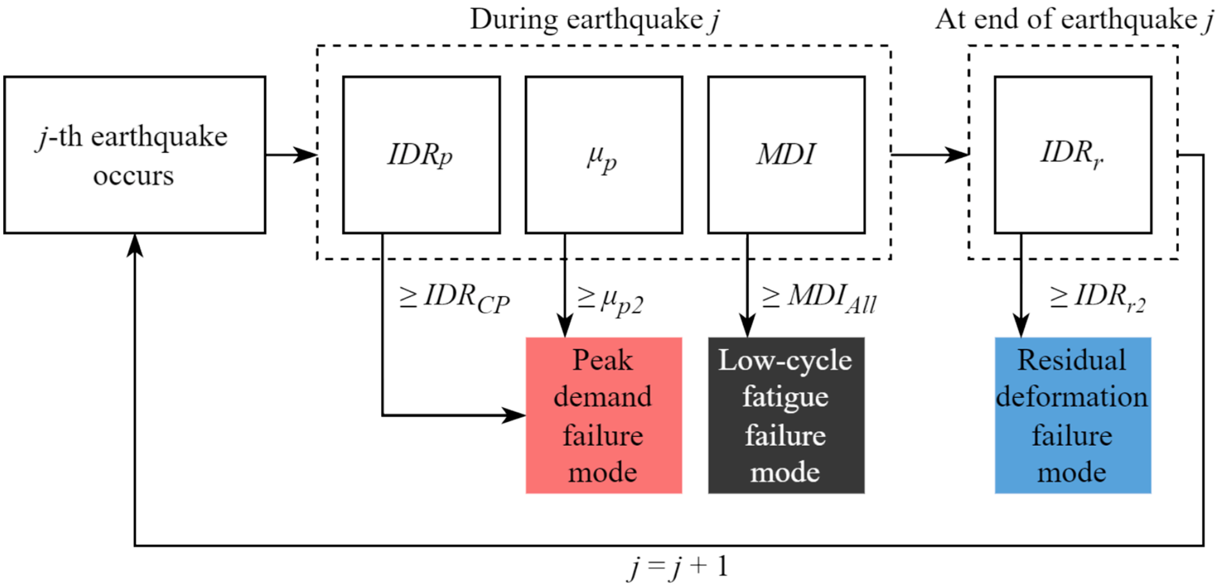

Fig. 14. Algorithm used to evaluate the probability of occurrence of a failure mode during each earthquake within t_L.

already occurred during earthquake $j-1$. Although this approach is useful to understand how probable each failure mode is, it is unlikely that the occurrence of a failure mode does not affect other failure modes. For example, a large residual drift in the structure exceeding IDR_{r2} at the end of earthquake j may result in the structure being judged as non-repairable and so in need of demolition and reconstruction. Thus, there would be no point in monitoring the occurrence of the BRBs' failure modes under the subsequent earthquakes, as the devices would be replaced along with the rest of the structure.

Therefore, it is of interest to re-evaluate the risks by considering the various failure modes as mutually exclusive, *i.e.*, the risk of occurrence of a given failure mode conditional on not having prior failure. The mutual exclusivity among failure modes is enforced not only when considering multiple earthquakes, but also within the same earthquake j, by performing the checks for each earthquake as illustrated in Fig. 14 and detailed below:

1. During the time history of the earthquake-induced motion, evaluate if:
   a. the structure collapses or experiences large damage in the MRF structure or BRBs as a consequence of peak demands. This failure mode is evaluated through the capacity limits IDR_{CP} and μ_{p2}, which represent the CP performance level in the MRF elements and the qualification ductility level for the BRB devices. It is herein referred to as 'peak demand' failure mode.
   b. any of the BRBs exceeds its low-cycle fatigue capacity. If this is the case, the whole structure is assumed to collapse. This failure mode, referred to as 'low-cycle fatigue' failure mode, is evaluated conservatively by considering the MDI_{All}, such that failure occurs if any BRB exceeds its capacity limit for any of the considered low-cycle fatigue models.
2. At the end of each motion, evaluate if the residual drifts compromise the repairability of the structure. This failure mode is evaluated through the capacity limit IDR_{r2} and it is referred to as 'residual deformation' failure mode.

The probability of occurrence of the i-th failure mode and of the system failure can be established respectively as:

$$P(D_i > C_i | t_L, NF_p) = \sum_{n=1}^{\infty} P(D_i > C_i | N = n, NF_p) \bullet P[N = n | t_L] \tag{10}$$

$$P(Failure | t_L, NF_p) = \sum_{i=1}^{4} P(D_i > C_i | t_L, NF_p) \tag{11}$$

where NF_p represents the condition of no other failure modes occurred in previous earthquakes or in the current one.

Fig. 15 shows the risk estimates for the case study structures and ground motion pools when considering the algorithm proposed in Fig. 14.

Consistently with the independent risk estimates, considering pulse-like ground motions rather than non-pulse-like motions heavily increases the risk of any failure, which moves from 1.74 to 4.86 % in R-4 and 5.36 to 9.45 % in R-6. Moreover, the risk of any failure mode for the R-6 BRB configuration is characterized by significantly higher levels of risk compared to the other configuration, when subjected to multiple ground motions.

Despite containing the envelope of six experimentally calibrated capacity models, the low-cycle fatigue failure mode (MDI_{All}) is negligible in all cases. If the Li et al. [18] model was to be considered alone, the risk values would result zero. The most critical model is Shi JianHua, as it results in the higher values of risk for the range of strain amplitudes of interest. This further reduction from the risk estimates considered for independent failure modes results from having observed other failure modes in previous earthquakes, as the low-cycle fatigue failure mode requires several ground motions to occur.

In general, the probability of residual deformation failure mode is the largest among the considered failure modes and is significantly larger when considering pulse-like earthquakes. This is especially interesting as the occurrence of this failure mode (and associated triggered actions, such as replacing the BRB devices) prevents the development of low-cycle fatigue failure mode in future earthquakes.

The probability of peak demand failure mode is significant in R-6 when subjected to pulse-like ground motions, with a probability of 3.19 %, which contrasts with the non-negligible risk of failure in the rest of the failure modes. Yet, being the peak demand failure mode the first condition to be evaluated in Fig. 14, it contains those cases in which an earthquake was paired with an extremely large IM as a result of the tail sampling on the hazard function.

By observing the low probability of low-cycle fatigue with respect to other failure modes, it can be argued that the replacement criteria for BRBs should solely focus on the damage resulting peak and residual

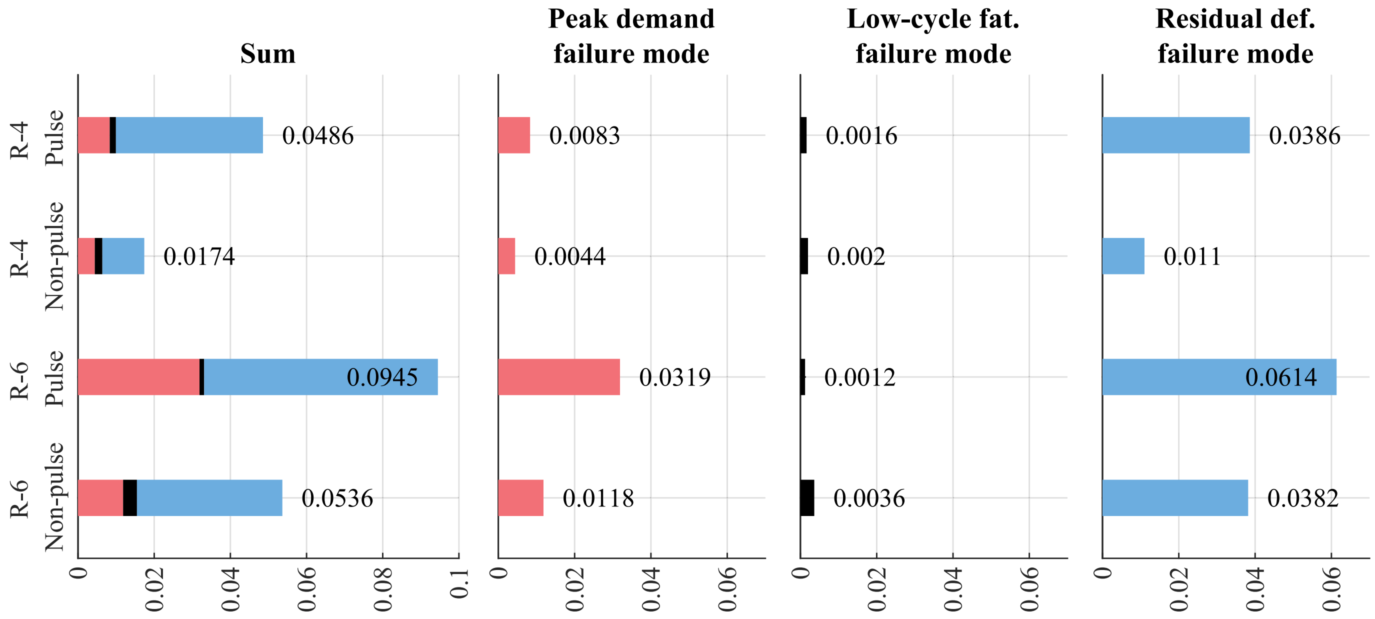

Fig. 15. Probability of a failure mode to occur given t_L, with considerations of the algorithm presented in Fig. 14.

demands. Replacing a BRB device to avoid future low-cycle fatigue in the aftermath of a strong earthquake is likely a conservative choice.

8. Conclusions

The present study evaluates the failure modes and seismic performance of steel dual Moment Resisting and Buckling-Restrained Braced Frames (MR-BRBFs) subjected to multiple earthquakes. These failure modes include low-cycle fatigue rupture of the BRBs, residual drifts of the structure, and peak quantities imposed on the BRBs and MRF components. All failure modes are evaluated by comparing the demand values with two or more capacity models and limits available in the literature.

Two case study structures, representative of a range of BRBs retrofitted frames, are used in this study. Finite element models of the frames are developed in OpenSees and subjected to multiple ground motion scenarios to capture cumulative demand parameters. The ground motion sequences are defined by a widely employed stochastic model for the earthquake occurrences during the design life of the structure, and their intensity distribution. Two ground motion pools containing, respectively, pulse- and non-pulse-like records are considered to define earthquake sequences consistent with the hazard model.

The results are presented in terms of risk estimates, *i.e.*, the probability of exceeding a capacity limit given the number of earthquakes n and the lifetime of the structure t_L. The failure modes are considered both independently of one another and as mutually exclusive, following a hierarchical order of occurrence.

The risk values observed for the low-cycle fatigue are already low when considering the failure modes independently, and they become negligible when considering mutually exclusive failure modes. This is a consequence of the higher probability of observing mutually exclusive failure modes in previous earthquakes, such as excessive residual drifts or excessive peak demands. This suggests that the replacing criteria for a BRB after a strong earthquake could be dependent solely on whether the peak and residual drifts observed are significant, without the need to monitor the low-cycle fatigue.

The pulse-like ground motion pools resulted in higher risk values for peak and residual failure modes, whereas no significant difference was observed for low-cycle fatigue.

Most of the risk estimates obtained for the case study structures exhibited a roughly linear growth with the number of earthquakes n when considering independent failure modes (refer to Fig. 12). This is likely influenced by the lack of initial stiffness degradation in the BRBs, however, it must be considered that for such structures it could be possible to define simplified strategies to account for the effects of multiple records. Nonetheless, such strategies could not be adequate for other structures experiencing significant degradation and where the seismic response is highly influenced by the state of the structure deriving from previous earthquakes.

The research outcomes are limited to the two investigated case study structures. However, such structures have been selected to have BRBs with significantly different response. In this context, the authors expect that the results can be generalized to a wide range of low-rise structures incorporating BRBs.

CRediT authorship contribution statement

Fernando Gutiérrez-Urzúa: Writing – review & editing, Writing – original draft, Visualization, Software, Methodology, Formal analysis, Conceptualization. **Fabio Freddi:** Writing – review & editing, Supervision, Methodology, Formal analysis, Conceptualization. **Enrico Tubaldi:** Writing – review & editing, Supervision, Methodology, Formal analysis, Conceptualization.

Declaration of competing interest

The authors declare that they have no known competing financial interests or personal relationships that could have appeared to influence the work reported in this paper.

Data availability

The data that has been used is confidential.

References

[1] Tremblay R, Poncet L, Bolduc P, Neville R, DeVall R. Testing and Design of Buckling Restrained Braces for Canadian Application. 13th World Conference on Earthquake Engineering, Vancouver, Canada; 2004.

[2] Zona A, Dall'Asta A. Elastoplastic model for steel buckling-restrained braces. J Constr Steel Res 2012;68:118–25. https://doi.org/10.1016/j.jcsr.2011.07.017.

[3] Freddi F, Tubaldi E, Zona A, Dall'Asta A. Seismic performance of dual systems coupling moment-resisting and buckling-restrained braced frames. Earthquake Eng Struct Dyn 2021;50:329–53. https://doi.org/10.1002/eqe.3332.

[4] Di Sarno L, Manfredi G. Seismic retrofitting with buckling restrained braces: Application to an existing non-ductile RC framed building. Soil Dyn Earthq Eng 2010;30:1279–97. https://doi.org/10.1016/j.soildyn.2010.06.001.

[5] Freddi F, Galasso C, Cremen G, Dall'Asta A, Sarno L, Giaralis A, et al. Innovations in earthquake risk reduction for resilience: recent advances and challenges. Int J Disaster Risk Reduct 2021;60:102267. https://doi.org/10.1016/j.ijdrr.2021.102267.

[6] Castaldo P, Tubaldi E, Selvi F, Gioiella L. Seismic performance of an existing RC structure retrofitted with buckling restrained braces. J Build Eng 2021;33. https://doi.org/10.1016/j.jobe.2020.101688.

[7] Della Corte G, D'Aniello M, Landolfo R. Field Testing of All-Steel Buckling-Restrained Braces Applied to a Damaged Reinforced Concrete Building. J Struct Eng 2015;141. https://doi.org/10.1061/(asce)st.1943-541x.0001080.

[8] Freddi F, Tubaldi E, Ragni L, Dall'Asta A. Probabilistic performance assessment of low-ductility reinforced concrete frames retrofitted with dissipative braces. Earthquake Eng Struct Dyn 2013;42:993–1011. https://doi.org/10.1002/eqe.2255.

[9] Guerrero H, Ruíz-García J, Escobar JA, Terán-Gilmore A. Response to seismic sequences of short-period structures equipped with Buckling-Restrained Braces located on the lakebed zone of Mexico City. J Constr Steel Res 2017;137:37–51. https://doi.org/10.1016/j.jcsr.2017.06.010.

[10] Hoveidae N, Tremblay R, Rafezy B, Davaran A. Numerical investigation of seismic behavior of short-core all-steel buckling restrained braces. J Constr Steel Res 2015;114:89–99. https://doi.org/10.1016/j.jcsr.2015.06.005.

[11] Qu B, Liu X, Hou H, Qiu C, Hu D. Testing of Buckling-Restrained Braces with Replaceable Steel Angle Fuses. J Struct Eng 2018;144. https://doi.org/10.1061/(asce)st.1943-541x.0001985.

[12] D'Aniello M, Della Corte G, Landolfo R. Finite Element Modelling and Analysis of "All-Steel" Dismountable Buckling Restrained Braces. TOBCTJ 2014;8:216–26. https://doi.org/10.2174/1874836801408010216.

[13] Fahnestock LA, Asce M, Ricles JM, Sause R. Experimental Evaluation of a Large-Scale Buckling-Restrained Braced Frame n.d. https://doi.org/10.1061/ASCE0733-94452007133:91205.

[14] Freddi F, Ghosh J, Kotoky N, Raghunandan M. Device uncertainty propagation in low-ductility RC frames retrofitted with BRBs for seismic risk mitigation. Earthq Eng Struct Dyn 2021;50:2488–509. https://doi.org/10.1002/eqe.3456.

[15] American Institute of Steel Construction. Seismic Provisions for Structural Steel Buildings (ANSI/AISC 341-16) 2016.

[16] Black C, Makris N, Aiken I. Pacific Earthquake Engineering Research Center Component Testing, Stability Analysis and Characterization of Buckling-Restrained Unbonded Braces (PEER Report 2002/08). 2002.

[17] Sabelli R. Research on Improving the Design and Analysis of Earthquake-Resistant Steel-Braced Frames. Earthquake Eng Res Inst 2001.

[18] Li C-H, Vidmar Z, Saxey B, Reynolds M, Uang C-M. A Procedure for Assessing Low-Cycle Fatigue Life of Buckling-Restrained Braces. J Struct Eng 2022;148. https://doi.org/10.1061/(asce)st.1943-541x.0003237.

[19] Xie L, Wu J, Huang Q. Experimental Study on Low-Cycle Fatigue Performance of Weld-Free Buckling-Restrained Braces. J Earthq Eng 2018;22:1392–414. https://doi.org/10.1080/13632469.2017.1286622.

[20] Takeuchi T, Ida M, Yamada S, Suzuki K. Estimation of Cumulative Deformation Capacity of Buckling Restrained Braces. J Struct Eng 2008;134:822–31. https://doi.org/10.1061/(ASCE)0733-9445(2008)134:5(822).

[21] Chen Q, Wang CL, Meng S, Zeng B. Effect of the unbonding materials on the mechanic behavior of all-steel buckling-restrained braces. Eng Struct 2016;111:478–93. https://doi.org/10.1016/j.engstruct.2015.12.030.

[22] Andrews BM, Fahnestock LA, Song J. Ductility capacity models for buckling-restrained braces. J Constr Steel Res 2009;65:1712–20. https://doi.org/10.1016/j.jcsr.2009.02.007.

[23] Manson SS. Behavior of Materials Under Conditions of Thermal Stress. National Advisory Committee for Aeronautics 1954.

[24] Coffin LF, Schenectady NY. A Study of the Effects of Cyclic Thermal Stresses on a Ductile. Metal 1954.

[25] Erochko J, Christopoulos C, Tremblay R, Choi H. Residual Drift Response of SMRFs and BRB Frames in Steel Buildings Designed according to ASCE 7-05. J Struct Eng 2011;137:589–99. https://doi.org/10.1061/(asce)st.1943-541x.0000296.

[26] McCormick J, Aburano H, Ikenaga M, Nakashima M. Permissible Residual Deformation Levels for Building Structures Considering Both Safety and Human Elements. The 14th World Conference on Earthquake Engineering, Beijing, China; 2008.

[27] Iwata Y, Hirokazu S, Kuwamura H. Reparability Limit of Steel Structural Buildings. J Struct Constr Eng 2005:165–72.

[28] Pieroni L, Freddi F, Latour M. Effective placement of self-centering damage-free connections for seismic-resilient steel moment resisting frames. Earthq Eng Struct Dyn 2022;51:1292–316. https://doi.org/10.1002/eqe.3615.

[29] Lettieri A, de la Peña A, Freddi F, Latour M. Damage-free self-centring links for eccentrically braced frames: development and numerical study. J Constr Steel Res 2023;201. https://doi.org/10.1016/j.jcsr.2022.107727.

[30] Federal Emergency Management Agency. Seismic Performance Assessment of Buildings Volume 1 - Methodology (FEMA P-58-1); 2018.

[31] Turchetti F, Tubaldi E, Patelli E, Castaldo P, Málaga-Chuquitaype C. Damage modelling of a bridge pier subjected to multiple earthquakes: a comparative study. Bull Earthq Eng 2023;21:4541–64. https://doi.org/10.1007/s10518-023-01678-y.

[32] Hoveidae N, Radpour S. Performance evaluation of buckling-restrained braced frames under repeated earthquakes. Bull Earthq Eng 2021;19:241–62. https://doi.org/10.1007/s10518-020-00983-0.

[33] Morfuni F, Freddi F, Galasso C. Seismic Performance of Dual Systems with BRBs under Mainshock-Aftershock Sequences, Seoul, South Korea: 2019.

[34] Veismoradi S, Cheraghi A, Darvishan E. Probabilistic mainshock-aftershock collapse risk assessment of buckling restrained braced frames. Soil Dyn Earthq Eng 2018;115:205–16. https://doi.org/10.1016/j.soildyn.2018.08.029.

[35] McKenna F, Fenves GL, Scott MH. Open System for Earthquake Engineering Simulation (OpenSees) 2000.

[36] Papadopoulos AN, Bazzurro P, Marzocchi W. Exploring probabilistic seismic risk assessment accounting for seismicity clustering and damage accumulation: Part I. Hazard analysis. Earthquake Spectra 2021;37:803–26. https://doi.org/10.1177/8755293020957338.

[37] Gupta A, Krawinkler H. Behavior of Ductile SMRFs at Various Seismic Hazard Levels. J Struct Eng 2000;126:98–107. https://doi.org/10.1061/(ASCE)0733-9445(2000)126:1(98).

[38] Gutiérrez-Urzúa F, Freddi F. Influence of the design objectives on the seismic performance of steel moment resisting frames retrofitted with buckling restrained braces. Earthq Eng Struct Dyn 2022;51:3131–53. https://doi.org/10.1002/eqe.3717.

[39] American Society of Civil Engineers. Seismic Evaluation and Retrofit of Existing Buildings (ASCE/SEI 41-17) 2017. https://doi.org/10.1061/9780784414859.

[40] Ragni L, Zona A, Dall'Asta A. Analytical expressions for preliminary design of dissipative bracing systems in steel frames. J Constr Steel Res 2011;67:102–13. https://doi.org/10.1016/j.jcsr.2010.07.006.

[41] Castro JM, Elghazouli AY, Izzuddin BA. Modelling of the panel zone in steel and composite moment frames. Eng Struct 2005;27:129–44. https://doi.org/10.1016/j.engstruct.2004.09.008.

[42] Gutiérrez-Urzúa F, Freddi F, Di Sarno L. Comparative analysis of code-based approaches for seismic assessment of existing steel moment resisting frames. J Constr Steel Res 2021;181. https://doi.org/10.1016/j.jcsr.2021.106589.

[43] United States Geological Survey (USGS). Unified Hazard Tool n.d. https://earthquake.usgs.gov/hazards/interactive/.

[44] Bozorgnia Y, Abrahamson NA, Atik LA, Ancheta TD, Atkinson GM, Baker JW, et al. NGA-West2 Research Project. Earthq Spectra 2014;30:973–87. https://doi.org/10.1193/072113EQS209M.

[45] Luzi L, Lanzano G, Felicetta C, D'Amico MC, Russo E, Sgobba S, et al. Engineering Strong Motion Database (ESM) (Version 2.0). Engineering Strong Motion Database (ESM) (Version 20) Istituto Nazionale Di Geofisica e Vulcanologia (INGV) 2020.

[46] Luzi L, Hailemikael S, Bindi D, Pacor F, Mele F, Sabetta F. ITACA (ITalian ACcelerometric Archive): A Web Portal for the Dissemination of Italian Strong-motion Data. Seismol Res Lett 2008;79:716–22. https://doi.org/10.1785/gssrl.79.5.716.

[47] Smerzini C, Galasso C, Iervolino I, Paolucci R. Ground motion record selection based on broadband spectral compatibility. Earthq Spectra 2014;30:1427–48. https://doi.org/10.1193/052312EQS197M.

[48] Baker JW. Quantitative classification of near-fault ground motions using wavelet analysis. Bull Seismol Soc Am 2007;97:1486–501. https://doi.org/10.1785/0120060255.

[49] Anderson JG. Quantitative Measure of the Goodness-of-Fit of Synthetic Seismograms. 13th World Conference on Earthquake Engineering, Vancouver, Canada: 2004.

[50] Kempton JJ, Stewart JP. Prediction equations for significant duration of earthquake ground motions considering site and near-source effects. Earthq Spectra 2006;22:985–1013. https://doi.org/10.1193/1.2358175.

[51] Iervolino I, Cornell CA. Record selection for nonlinear seismic analysis of structures. Earthq Spectra 2005;21:685–713. https://doi.org/10.1193/1.1990199.

[52] Zacharenaki A, Fragiadakis M, Assimaki D, Papadrakakis M. Bias assessment in Incremental Dynamic Analysis due to record scaling. Soil Dyn Earthq Eng 2014;67:158–68. https://doi.org/10.1016/j.soildyn.2014.09.007.

[53] Tremblay R, Bolduc P, Neville R, DeVall R. Seismic testing and performance of buckling-restrained bracing systems. Can J Civ Eng 2006;33:183–98. https://doi.org/10.1139/l05-103.

[54] Ma N, Wu B, Zhao J, Li H, Ou J, Yang W. Full Scale Test of All-Steel Buckling Restrained Braces. The 14th World Conference on Earthquake Engineering, Beijing, China: 2008.

[55] American Society for Testing and Materials. Practices for Cycle Counting in Fatigue Analysis (ASTM E1049-85) 2017. https://doi.org/10.1520/E1049-85R17.

[56] Tong C, Wu J, Hua K, Xie L. Low-Cycle Fatigue Life Estimation Curve for Buckling-Restrained Braces Based on Cumulative Plastic Deformation. J Earthq Eng 2022;26:2773–801. https://doi.org/10.1080/13632469.2020.1772152.